Helmholtz-Zentrum Geesthacht
Zentrum für Material- und Küstenforschung

Final Draft
of the original manuscript:

Wozniak, E.; Spirkova, M.; Slouf, M.; Haramus, V.M.; Safarikova, M.; Safarik, I.; Stepanek, M.:

Stabilization of aqueous dispersions of poly(methacrylic acid)-coated iron oxide nanoparticles by double hydrophilic block polyelectrolyte poly(ethylene oxide)-block-poly(N-methyl-2-vinylpyridinium iodide)

In: Colloids and Surfaces A (2016) Elsevier

DOI: 10.1016/j.colsurfa.2016.11.044

Stabilization of aqueous dispersions of poly(methacrylic acid)-coated iron oxide nanoparticles by double hydrophilic block polyelectrolyte poly(ethylene oxide)-*block*-poly(*N*-methyl-2-vinylpyridinium iodide)

Edyta Woźniak[1,2], Milena Špírková,[3] Miroslav Šlouf,[3] Vasil M. Garamus,[4] Mirka Šafaříková,[5] Ivo Šafařík[5] and Miroslav Štěpánek[1,*]

[1]*Department of Physical and Macromolecular Chemistry, Faculty of Science Charles University in Prague, Hlavova 2030, 12840 Prague 2, Czech Republic*

[2]*Department of Chemistry, The Faculty of Food Science, Wrocław University of Environmental and Life Sciences, C. K. Norwida 25, 50-375 Wrocław, Poland*

[3]*Institute of Macromolecular Chemistry, Academy of Sciences of the Czech Republic, Heyrovský Sq. 2, 16206 Prague 6, Czech Republic*

[4]*Helmholtz-Zentrum Geesthacht, Centre for Materials and Coastal Research, Max-Planck-Str. 1, D-21502 Geesthacht, Germany*

[5]*Department of Nanobiotechnology, Biology Centre, ISB, CAS, Na Sádkách 7, 370 05 České Budějovice, Czech Republic*

*Corresponding author. e-mail: stepanek@natur.cuni.cz

Abstract. Aqueous dispersions of poly(methacrylic acid)-coated superparamagnetic iron oxide nanoparticles (PMAA@SPIONs) and nanoparticles obtained by adding a layer of double-hydrophilic cationic block polyelectrolyte poly(ethylene oxide)-*block*-poly(N-methyl-2-vinylpyridinium iodide) (PEO-QP2VP) on PMAA@SPIONs were studied by a combination of static and dynamic light scattering, SAXS, transmission electron microscopy and atomic force microscopy, probing the structure of the SPION aggregates on the lengthscale from 1 to 10^3 nm. Both SALS and AFM results indicate that adding a PEO-QP2VP layer to PMAA@SPIONs decreases the size of SPION aggregates formed in the dispersions. While TEM micrographs show that PEO-QP2VP@PMAA@SPION particles are less apt to form small clusters with the size of several tens nm compared to PMAA@SPION particles, the local clustering has no effect on the power law scattering behavior ($I(q) \sim q^{-1.4}$) of the SPION dispersions at longer lengthscales (tens to hundreds nm), which reflects mainly polydispersity of the aggregates.

1. Introduction

Superparamagnetic nanoparticles (NPs), mostly based on iron oxides magnetite (Fe_3O_4) or maghemite (γ-Fe_2O_3), have received much attention in the past decade due to multiple potential applications in pharmacology as both therapeutic and diagnostic ("theranostic") agents [1–3], including their use in targeted drug delivery systems [4] allowing for manipulation by external magnetic field, as contrast agents for magnetic resonance imaging [5] or for cancer treatment by magnetic heating therapy [6]. In highly concentrated dispersions of magnetic nanoparticles, dispersant liquid moves together with NPs in the direction of external magnetic field so that the dispersions behave like magnetic fluids (ferrofluids) [7].

For all these applications it is essential to prepare stable aqueous dispersions of magnetic nanoparticles. A common procedure for synthesis of superparamagnetic iron oxide nanoparticles (SPIONs) is precipitation of Fe^{2+} and Fe^{3+} ions in alkaline aqueous solution at elevated temperature (hydrothermal synthesis) [8] in the presence of compounds adsorbing on the formed iron oxide phase in the course of the reaction and preventing SPION nanocrystals from coagulation and aggregation. A broad variety of compounds have been used as coating agents such as surfactants [9], dextran [10], starch [11], chitosan derivatives [12], polyethylene glycol [13] or poly(acrylic acid) (PAA) [14] and poly(methacrylic acid) (PMAA) [15]. Pendant COOH groups of PAA or PMAA provide both covalent binding to iron oxide and solvation of the coated particles. Recently, we described a simple hydrothermal synthesis of PMAA-coated SPIONs (PMAA@SPIONs) and preparation of hybrid magnetic material for immobilization of various biologically active species (yeast cells, enzymes) based on the chitosan/PMAA@SPIONs system and the formation of the interpolyelectrolyte complex of PMAA with chitosan [16].

Ferrofluids undergo aggregation even in dilute dispersions due to long range magnetic interactions between the magnetic nanoparticles [17]. Therefore it is desirable to develop coating agents that provide good solvation of the NPs and will act as spacer preventing them from aggregation. Block copolymers one block of which binds to NP surface and the other forms the hydrated protective corona which provides the steric stabilization represent a class of such spacers [18,19]. NPs coated by a charged agent can be stabilized by an additional layer of a double hydrophilic block polyelectrolyte (DHBP) consisting of a neutral hydrophilic block and an oppositely charged polyelectrolyte block [20]. In this article, we use a combination of scattering (SAXS, light scattering, small-angle light scattering) and

microscopy (TEM, AFM) techniques to study the size and structure of the aggregates formed in PMAA@SPIONs aqueous dispersions and the influence of the secondary coating of PMAA@SPIONs by cationic DHBP poly(ethylene oxide)-*block*-poly(N-methyl-2-vinylpyridinium iodide) (PEO-QP2VP) on the aggregation, including both the cluster formation at the nanometer scale and the overall size of the aggregates in the range of micrometers.

2. Experimental

2.1. Materials

2.1.1. Chemicals

Poly(methacrylic acid), sodium salt (PMAA, 30 wt. % solution in water, M_w = 9.5 kg mol^{-1}), $FeCl_3.6H_2O$ and $FeCl_2.4H_2O$ were from Sigma-Aldrich (St. Louis, MO, USA). Poly(ethylene oxide)-*block*-poly(N-methyl-2-vinylpyridinium iodide) (PEO-QP2VP), M_w(PEO) = 5.9 kg mol^{-1}, M_w(QP2VP) = 56.5 kg mol^{-1}, degree of quaternization 86%, was obtained from Polymer Source (Dorval, Quebec, Canada). Other chemicals were obtained from Lachner (Neratovice, Czech Republic).

2.1.2. Preparation of PMAA-stabilized superparamagnetic iron oxide nanoparticles (PMAA@SPIONs)

PMAA solution (25 mL) was mixed with 50 mL of 2M HCl. Ferric chloride (5.0 g) and ferrous chloride (2.1 g) were dissolved together in 13 mL of 2M HCl. Both solutions were mixed using a RZR 2041 mechanical stirrer (Heidolph Instruments, Schwabach, Germany) at 465 rpm and heated on a water bath to 60 °C. Then 75 mL of 7.5 % ammonium hydroxide solution was added dropwise under mixing. The formed ferrofluid was then incubated at 60 °C for the next 15 min. Free ammonium gas was allowed to evaporate at room temperature in a fume hood for 24 hours and then the ferrofluid was centrifuged at 5000 rpm for 45 min using a Hettich Universal 320 centrifuge (Andreas Hettich, Tuttlingen, Germany). In order to increase the iron oxide nanoparticle concentration in the ferrofluid, water was evaporated at room temperature in a fume hood for several days. The final concentrations of iron oxide and in the resulting dispersion was 70 mg mL^{-1} The molar amount of methacrylate units per 1 mg of iron oxide in the dispersion was 27 mmol.

2.1.3. Coating of PMAA@SPIONs with PEO-QP2VP

PMAA@SPION dispersions diluted with 0.01 M NaCl (iron oxide concentrations 0.05, 0.1, 0.2 and 0.5 mg mL^{-1}) were mixed with various amounts of 10 mg mL^{-1} stock solution of QP2VP-PEO in 0.01 M NaCl, so that the final concentrations of PEO-QP2VP in the dispersions were 0, 0.01, 0.1, 0.25 and 0.5 mg mL^{-1}. Since the molar amount of 2-vinylpyridinium units per 1 mg of the copolymer is 3.5 mmol, the charge ratio *Z*, corresponding to the molar ratio of 2-vinylpyridinium and methacrylate units, Z = [Q2VP]/[MAA], ranged from 0 to 2.5. The pH of the dispersions ranged from 8.0 to 8.3 ensuring full ionization of PMAA chains. The dispersions were left overnight at room temperature for equilibration prior to measurements.

2.2. Characterization techniques

2.2.1. Wide-angle light scattering

The light scattering setup (ALV, Langen, Germany) for combined static and dynamic multiangle light scattering measurements consisted of a 22 mW He-Ne laser, operating at the wavelength, λ = 632.8 nm, an ALV CGS/8F goniometer, an ALV High QE APD detector and an ALV 5000/EPP multibit, multitau autocorrelator. The measurements were carried out at 25°C at the PMAA@SPION concentrations, c_{NP} = 0.5 mg mL^{-1}. The scattering angles, θ, ranging from 30° to 150°, corresponding to the scattering vector magnitudes, $q=(4\pi n_0/\lambda)\sin(\theta/2)$ (here n_0 is the refractive index of the solvent), from 6×10^{-3} to 0.025 nm^{-1}. DLS measurements were evaluated by fitting the measured normalized time autocorrelation function of the scattered light intensity, $g^{(2)}(t,q)$, related to the electric field autocorrelation function, $g^{(1)}(t,q)$, by the Siegert relation, $g^{(2)}(t,q)=1+\beta|g^{(1)}(t,q)|^2$. The data were fitted (i) with the aid of the constrained regularization algorithm (CONTIN) which provides the distribution of relaxation times τ, $A(\tau,q)$, as the inverse Laplace transform of $g^{(1)}(t,q)$ function

$$g^{(1)}(t,q)=\int_0^\infty A(\tau,q)\exp\left(-\frac{t}{\tau}\right)\mathrm{d}\tau \qquad (1)$$

and (ii) using the 2nd order cumulant expansion

$$\ln g^{(1)}(t,q) = -\Gamma_1(q)t + \frac{\Gamma_2(q)}{2}t^2, \quad (2)$$

where $\Gamma_1(q)$ and $\Gamma_2(q)$, respectively, are the first and the second moment of the distribution function of the relaxation rates. For fluctuations caused by translation diffusion of scatterers, both techniques provide the corresponding apparent diffusion coefficient at the given q either as the distribution function ($D_{app} = 1/\tau q^2$) or as the mean value ($\langle D_{app} \rangle = \Gamma/q^2$).

2.2.2. Small-angle light scattering

SALS measurements were performed with a Mastersizer 3000 instrument (Malvern, U.K.) equipped with a Hydro SV dispergation unit. The data were carried out in the q range from 5×10^{-4} to 9×10^{-3} nm^{-1}. Obtained scattering curves were averages of 3 subsequent measurements, each of which took 10 s.

2.2.3. Electrophoretic light scattering

ζ-Potential measurements were carried out with a Nano-ZS Zetasizer (Malvern Instruments, U.K.). ζ-Potential values were calculated from electrophoretic mobilities (average of three subsequent measurements, each of which consisted of 15–100 runs) using the Henry equation in the Smoluchowski approximation, $\mu = \varepsilon\zeta/\eta$, where μ is the electrophoretic mobility and ε is the dielectric constant of the solvent.

2.2.4. Small-angle X-ray scattering (SAXS)

SAXS experiments were carried out on the P12 BioSAXS beamline at the PETRA III storage ring (EMBL/DESY, Hamburg, Germany) at 20°C. The beamline was equipped with a Pilatus 2M detector and synchrotron radiation with a wavelength of λ = 0.1 nm. The sample-detector distance was 3 m, permitting coverage of the q-range interval from 0.07 to 4.4 nm^{-1}. The q-range was calibrated using the diffraction patterns of silver behenate. The experimental data were normalized to the transmitted beam intensity and corrected for nonhomogeneous detector response and the background scattering of the solvent was subtracted. The solvent scattering was measured before and after the sample scattering (c_{NP} = 0.5 mg mL^{-1}) to control for possible sample holder contamination. 20 consecutive frames with 0.05 s exposures comprising measurement of the solvent, sample, and solvent were performed. The data were

checked for radiation damage. The final scattering curves were obtained by automated data acquisition software [21], recalculated to absolute scattering intensities using the forward scattering of 3.6 mg mL^{-1} bovine serum albumin in 50 mM HEPES pH 7.5 buffer, assuming $(I(0)/c)_{BSA}$ = 4.84×10^{-2} cm^2 mg^{-1} [22] and fitted using SASfit 0.94.7 software [23]. An automatic sample changer was used for a sample volume of 20 μL and cleaning-filling cycle of 1 min.

2.2.5. Transmission electron microscopy

Transmission electron microscopy (TEM) measurements were performed with a Tecnai G2 Spirit Twin microscope (FEI, Czech Republic). The samples were prepared as follows: 2 μl of the SPION dispersion (c_{NP} = 0.5 mg mL^{-1}) were dropped onto a standard carbon-coated copper grid, left to equilibrate for 1 min at ambient temperature and then the excess of the dispersion was sucked off by touching the bottom of the grid with a thin strip of a filter paper. The sample was left to dry completely at ambient temperature and then visualized in the microscope using bright-field imaging (TEM/BF) at accelerating voltage of 120 kV.

2.2.6. Atomic force microscopy

Atomic force microscopy (AFM) measurements were performed with a Dimension Icon microscope (Bruker), equipped with a SSS-NCL probe, a Super Sharp SiliconTM SPM Sensor (NanoSensorsTM Switzerland; spring constant 35 N m^{-1}, resonant frequency ~170 kHz). Measurements were performed under ambient conditions using the tapping mode AFM technique. Samples were prepared by fast dip coating of freshly peeled out mica (flogopite, $KMg_3(Si_3Al)O_{10}(OH)_2$) in PMAA@SPION or PEO-QP2VP@PMAA@SPION dispersions (c_{NP} = 0.5 mg mL^{-1}), diluted with tenfold volume of deionized water. After water evaporation, the samples were dried in a vacuum oven at ambient temperature for 12 h.

3. Results and discussion

PMAA@SPION particles prepared according to the procedure described in Section 2.1.1 were characterized previously by TEM including selected area electron diffraction (SAED), DLS and small-angle neutron scattering (SANS) [16]. While SAED measurements

confirmed magnetite/maghemite structure of the SPION nanocrystals, TEM and scattering measurements showed that PMAA@SPION particles form large clusters in aqueous solution (DLS revealed scatterers with hydrodynamic radii about 100 nm).

In this article, we investigated PMAA@SPION and PEO-QP2VP@PMAA@SPION aqueous dispersions by a combination of SAXS, SLS and SALS measurements covering the q-range from 5×10^{-4} to 5 nm^{-1} corresponding to Bragg lengths from 1.3×10^{4} to 1.3 nm. Combined SAXS/SLS/SALS curves for PMAA@SPION and PEO-QP2VP@PMAA@SPION dispersions (Z=0.13) in 0.01 M aqueous NaCl are shown in Fig. 1. In contrast to SANS, scattering length density of iron oxide core of the nanoparticles in SAXS is much larger than that of the polymer coating so that the SAXS curve reveals mostly scattering from bare iron oxide particles. Similarly to what was found previously by SANS for the PMAA@SPION system, the curve shows two power law regimes, one in the high q range (1 – 3 nm^{-1}) reflecting the scattering of the individual SPIONs, and the second in the low q range (0.004 – 0.4 nm^{-1}) with the exponent ca. –1.4 which corresponds to the internal structure of the aggregates. The size of the magnetic nanoparticles can be estimated from the Bragg lengths corresponding to the q range of the crossover regime between the two power law regimes (0.4 – 1 nm^{-1}) as ca. 6–15 nm.

The entire SAXS/SLS/SALS curve can be fitted by the model in which the scattering of individual SPIONs is described by the Fisher-Burford approximant [24] limiting to the Guinier law at $q \to 0$ and to the power law at $q \to \infty$, and the attractive interactions between SPIONs are described by the mass fractal structure factor with the exponential cut-off of the pair-distance distribution function, $g(R) = (d/4\pi\Phi r^d)R^{d-3}\exp(-R/\xi)+1$, where Φ is the mean particle density, d is the mass fractal dimension of the cluster, r is the characteristic dimension of the particles forming the clusters and ξ is the cut-off length related to the gyration radius of the aggregates as $\xi^2 = 2R_g^2/D(D+1)$ [25]. The scattering function then reads

$$I(q) = N(\Delta b)^2 \left\{ 1 + \frac{d\Gamma(d-1)\sin\left[(d-1)\arctan(q\xi)\right]}{(qr)^d (1+q^{-2}\xi^{-2})^{(d-1)/2}} \right\} \left(1 + \frac{2}{3D} q^2 s^2 \right)^{-D/2} \qquad (3)$$

where N is the number density and Δb is the scattering length of the clusters, s is the gyration radius of the particles forming the cluster and D the exponent for the power-law scattering of the particles. The fits (solid lines in Fig. 1) provide the values of parameters summarized in Table 1.

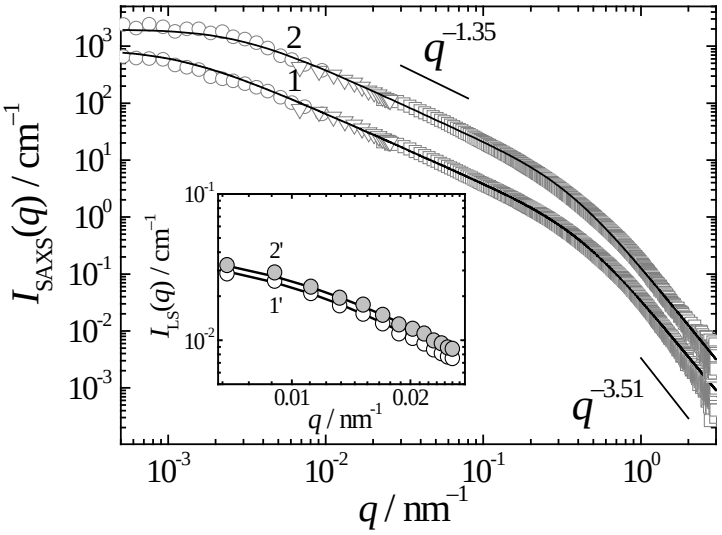

Fig. 1. Combined SALS (circles), SLS (triangles) and SAXS (squares) curves for PMAA@SPION (curve 1) and QP2VP-PEO@PMAA@SPION (curve 2) dispersions. SALS and SLS scattering intensities are rescaled to the SAXS absolute scale. The curve 2 is shifted by a multiplicative factor of 5 for better readability. The PMAA@SPION concentration in both dispersions was 0.5 mg/mL, the QP2VP-PEO concentration in the QP2VP-PEO@PMAA@SPION was 0.5 mg/mL, which corresponds to the ratio between the molar amounts of PMAA and QP2VP units in the system, $Z = 0.13$. Insert: SLS curves for PMAA@SPION (curve 1') and QP2VP-PEO@PMAA@SPION (curve 2') on the SLS absolute scale.

	ξ, nm	d	r, nm	s, nm	D
PMAA@SPION	1040±16	1.35±0.01	4.90±0.01	5.16±0.07	3.51±0.01
PEO-QP2VP@PMAA@SPION	414±7	1.35±0.01	5.20±0.01	6.39±0.08	3.40±0.02

Table 1. Parameters of the fits of SALS/SLS/SAXS data with eq. 2.

While the previously reported SANS data were strongly influenced by scattering contribution from PMAA chains in the coating layer, SAXS scattering is dominated by the contribution from iron oxide cores due to difference in contrast which is ~50 times higher for iron oxide than for the polymer. This is why the power law exponent in the SPION form factor is higher than 3 indicating that the scattering in the high q regime occurs at SPION interfaces. The power law exponent in the low q regime is somewhat lower than what would be expected to diffusion-limited cluster aggregation probably as a result of polydispersity of the aggregates. This assumption is supported by the DLS measurements (Fig. 2) showing that the distributions of hydrodynamic radii of the aggregates are very broad which results also in the strongly q-dependent apparent diffusion coefficients. It is worth mentioning that values of the exponent close to 1 were reported earlier for SPION aggregates in aqueous dispersions

[20,26] and it was suggested that the low mass fractal dimensions of the aggregates in such systems can be caused also by the formation of wormlike structures due to dipolar magnetic interactions between small SPION clusters. This hypothesis, however, is not supported by the results of TEM or AFM measurements.

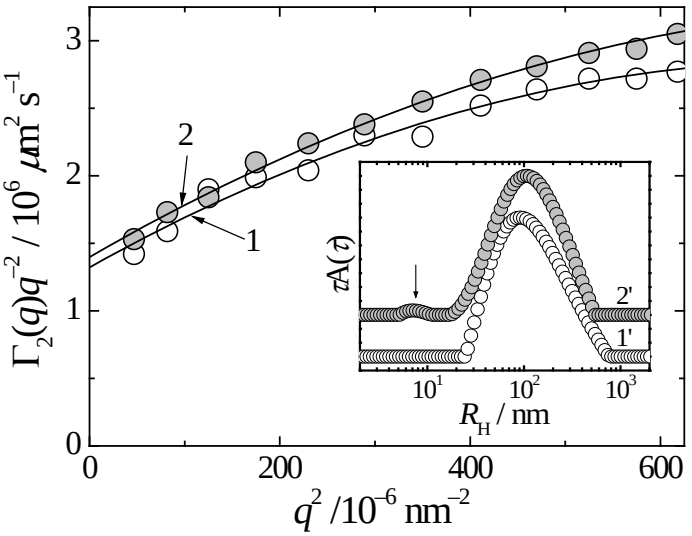

Fig. 2. Apparent diffusion coefficients from DLS measurements of PMAA@SPION (curve 1) and QP2VP-PEO@PMAA@SPION (curve 2) dispersions as functions of q^2. Insert: DLS CONTIN distributions of hydrodynamic radii at $\theta = 90°$ for PMAA@SPION (curve 1') and QP2VP-PEO@PMAA@SPION (curve 2')

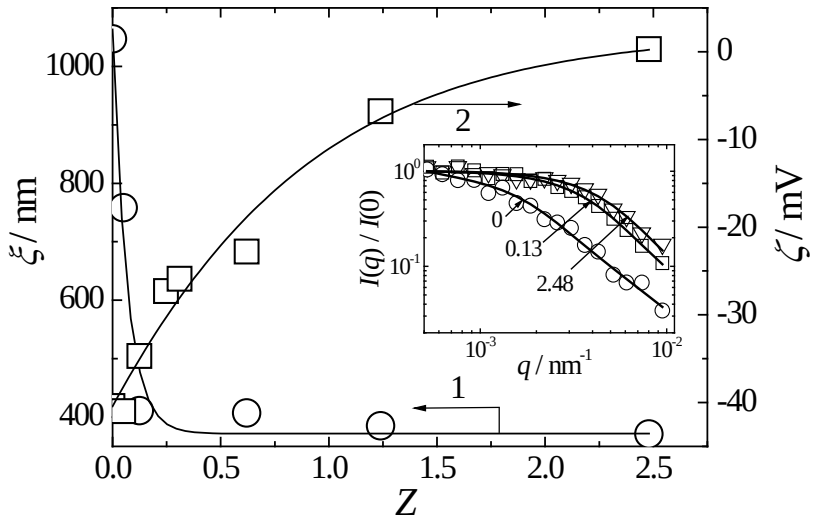

Fig. 3. Cut-off length, ξ (curve 1) and ζ-potential (curve 2) of PEO-QP2VP@PMAA@SPIONs aggregates as function of charge ratio, Z. Insert: SALS curves of PEO-QP2VP@PMAA@SPIONs at various Z ratios (indicated at the individual curves) between the molar amounts of PMAA and QP2VP units in the system.

The scattering curves differ distinctly in the cut-off length ξ, which means that PEO-QP2VP@PMAA@SPIONs form smaller aggregates than PMAA@SPIONs indicating that the coating by the additional layer of PEO-QP2VP suppresses the aggregation. Fig. 3 shows that the cut-off length of aggregates (curve 1) in PEO-QP2VP@PMAA@SPIONs dispersions decreases with the increasing amount of PEO-QP2VP adsorbed on PMAA@SPIONs (the corresponding SALS curves are shown as insert of Fig. 3). The negative ζ-potential of the particles (curve 2) increasing to zero confirms binding of positively charged PEO-QP2VP on the negatively charged PMAA@SPIONs surface and indicates that the dispersion becomes sterically stabilized. Apparent hydrodynamic radii about 100 nm obtained from DLS are much lower than the cut-off lengths of the aggregates from SALS which is partly due to the polydispersity of the aggregates (z-average of R_g^2 vs. z-average of R_H^{-1}), partly due to the fact that the aggregates are loose and the DLS measurements reflect rather the internal dynamics of the aggregates than their diffusive motions. However, even the DLS measurements indicate that the mean hydrodynamic radius of PEO-QP2VP@PMAA@SPIONs aggregates calculated from $\Gamma_1(q)/q^2$ extrapolated to $q \rightarrow 0$ (156 nm) is slightly lower than that of PMAA@SPIONs aggregates (165 nm). Moreover, an additional fast mode with the mean apparent R_H of 7 nm appears in the DLS distribution of hydrodynamic radii in the case of PEO-QP2VP@PMAA@SPIONs dispersions, indicating diffusion of single SPIONs.

The influence of PEO-QP2VP coating of PMAA@SPIONs can also be followed by microscopic techniques which confirm the results from scattering measurements. AFM images (Fig. 4) show that the average size of the aggregates deposited on the mica surface decreases with the increasing amount of PEO-QP2VP in the system. TEM micrographs of PMAA@SPIONs and PEO-QP2VP@PMAA@SPIONs nanoparticles in Fig. 5 indicate that the tendency of SPIONs to form clusters is suppressed by adding a PEO-QP2VP layer to PMAA@SPIONs.

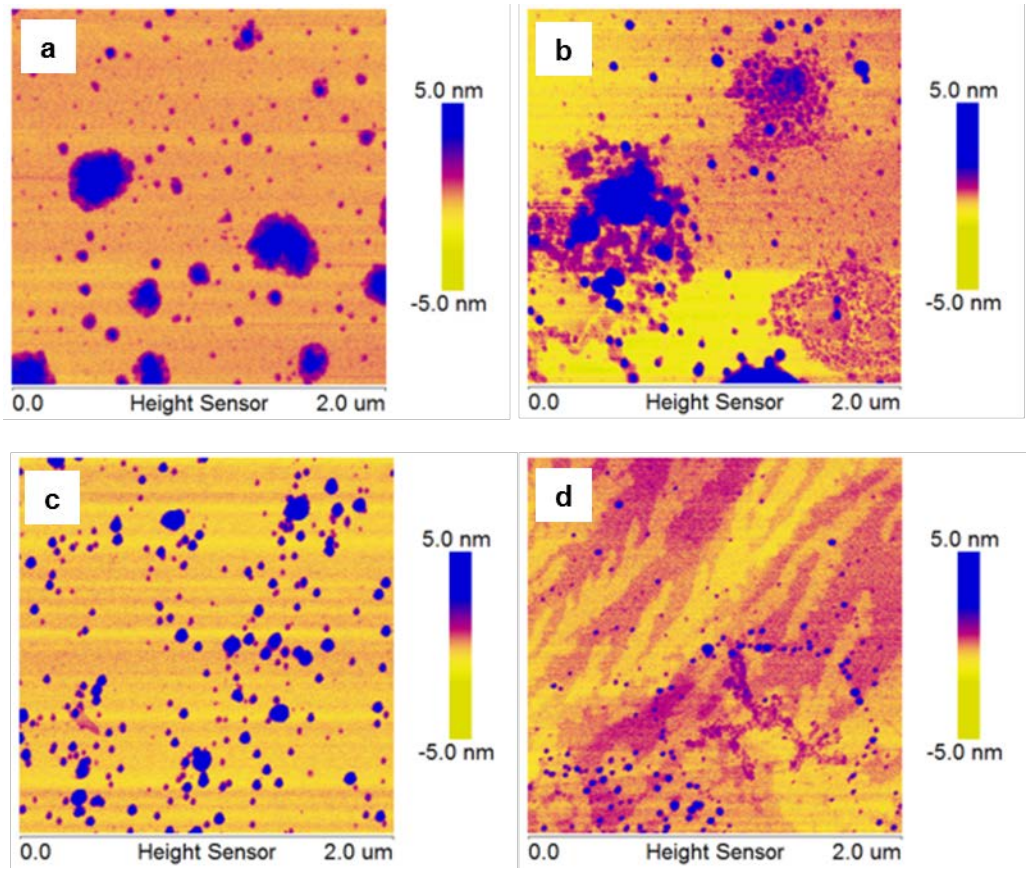

Fig. 4. AFM height scans (2 μm × 2 μm) of PEO-QP2VP@PMAA@SPIONs aggregates deposited at freshly cleaved-off mica surface at (a) Z = 0, (b) 0.03, (c) 0.06 and (d) 0.12.

It is noteworthy that our previous study [20] of the interaction of oleate@SPIONs with QNPHOS-PEO copolymer showed that while QNPHOS-PEO suppresses formation of the large aggregates, it promotes local clustering at smaller length scales, which is observed by both TEM and DLS measurements. The reason for this difference between PEO-QP2VP@PMAA@SPIONs and QNPHOS-PEO@oleate@SPIONs probably stems in (i) a higher negative ζ-potential of oleate@SPIONs, –80 mV, compared to ca. –40 mV of PMAA@SPIONs and (ii) higher charge density of QNPHOS chains (two positive charges per monomeric unit) compared to PEO-QP2VP. While in the case of the oleate@SPIONs, the nanoparticles are efficiently electrostatically stabilized by the oleate layer and the addition of QNPHOS-PEO leads to bridging of the SPIONs and formation of SPION clusters, in the case of oleate@SPIONs, large clusters are formed due to the inefficient stabilization by the PMAA layer and disrupted by the addition of the PEO-QP2VP layer.

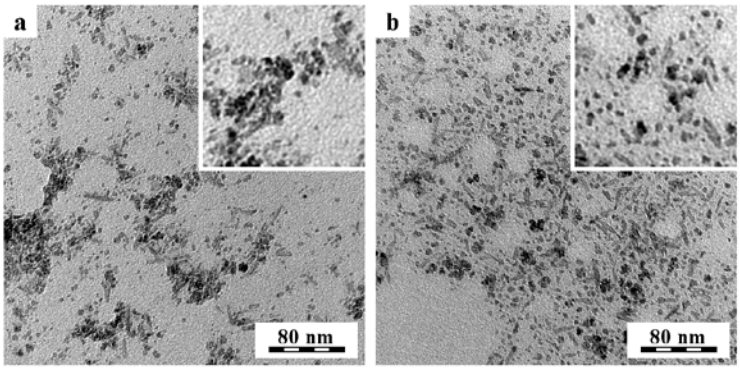

Fig. 5. TEM images of (a) PMAA@SPIONs and (b) PEO-QP2VP@PMAA@SPION aggregates. Inserts show magnified images (100 nm × 100 nm) of the SPIONs clusters.

4. Conclusions

We have found that the coating of PMAA@SPIONs with an additional layer of the double hydrophilic block polyelectrolyte (DHBP) PEO-QP2VP (i) suppresses the clustering of the magnetic nanoparticles in aqueous dispersions on the nm scale (comparable with the size of the SPIONs) and (ii) reduces the size of SPION aggregates in aqueous dispersions ranging from several hundreds to several thousands of nm. These results confirm that the coating of electrostatically stabilized SPIONs by DHBPs improves the stability of the SPIONs aqueous dispersions. SAXS and light scattering show that the internal structure of the aggregates in the q range from 0.004 to 0.4 nm^{-1} can be described by the power law scattering behavior $I(q) \sim q^{-1.4}$ for both PMAA@SPION and PEO-QP2VP@PMAA@SPION aggregates, indicating a very loose structure of the aggregates independent of the amount of the added PEO-QP2VP. The observed power law scattering behavior is most probably affected by polydispersity of the aggregates.

Acknowledgment

Edyta Woźniak, Ivo Šafařík, Mirka Šafaříková and Miroslav Štěpánek acknowledge the support from the Czech Science Foundation (grant 14-11516S). Electron microscopy at the Institute of Macromolecular Chemistry was supported by projects TE01020118 (Technology Agency of the Czech Republic) and POLYMAT LO1507 (Ministry of Education, Youth and Sports of the CR, program NPU I). The support of Clement Blanchet (EMBL) is kindly acknowledged.

References

[1] J.R. McCarthy, R. Weissleder, Multifunctional magnetic nanoparticles for targeted imaging and therapy, Adv. Drug Delivery Revs. 60 (2008) 1241–1251.
[2] O. Veiseh, J.W. Gunn, M.Q. Zhang, Design and fabrication of magnetic nanoparticles for targeted drug delivery and imaging, Adv. Drug Delivery Revs. 62 (2010) 284–304.
[3] D. Yoo, L.H. Lee, T.H. Shin, J. Cheon, Theranostic Magnetic Nanoparticles, Acc. Chem. Res. 44 (2011) 863–874.
[4] X.B. Mou, Z.S. Ali, S. Li, N.Y. He, Applications of Magnetic Nanoparticles in Targeted Drug Delivery System, J. Nanosci. Nanotechnol. 15 (2015) 54–62.
[5] J.H. Lee, Y.M. Huh, Y. Jun, J. Seo, J. Jang, H.T. Song, S. Kim, E.J. Cho, H.G. Yoon, J.S. Suh, J. Cheon, Artificially engineered magnetic nanoparticles for ultra-sensitive molecular imaging, Nature Med. 13 (2007) 95–99.
[6] K.H. Bae, M. Park, M.J. Do, N. Lee, J.H. Ryu, G.W. Kim, C. Kim, T.G. Park, T. Hyeon, Chitosan Oligosaccharide-Stabilized Ferrimagnetic Iron Oxide Nanocubes for Magnetically Modulated Cancer Hyperthermia, ACS Nano 6 (2012) 5266–5273.
[7] S. Odenbach, Ferrofluids – magnetically controlled suspensions, Colloids Surf. A Physicochem. Eng. Aspects 217 (2003) 171–178.
[8] S. Ge, X.Y. Shi, K. Sun, C.P. Li, C. Uher, J.R. Baker, M.M.B. Holl, B.G. Orr, Facile Hydrothermal Synthesis of Iron Oxide Nanoparticles with Tunable Magnetic Properties, J. Phys. Chem. C 113 (2009)13593–13599.
[9] D.K. Kim, Y. Zhang, W. Voit, K.V. Rao, M. Muhammed, Synthesis and characterization of surfactant-coated superparamagnetic monodispersed iron oxide nanoparticles, J. Magn. Magn. Mater. 225 (2001) 30–36.
[10] X.Q. Xu, H. Shen, J.R. Xu, J. Xu, X.J. Li, X.M. Xiong, Core-shell structure and magnetic properties of magnetite magnetic fluids stabilized with dextran, Appl. Surf. Sci. 252 (2005) 494–500.
[11] J.S. Jiang, Z.F. Gan, Y. Yang, B. Du, M. Qian, P. Zhang, A novel magnetic fluid based on starch-coated magnetite nanoparticles functionalized with homing peptide, J. Nanopart. Res. 11 (2009) 1321–1330.
[12] Z.T. Tsai, F.Y. Tsai, W.C. Yang, J.F. Wang, C.L. Liu, C.R. Shen, et al., Preparation and characterization of ferrofluid stabilized with biocompatible chitosan and dextran sulfate hybrid biopolymer as a potential magnetic resonance imaging (MRI) T2 contrast agent, Mar. Drugs 10 (2012) 2403–2414.

[13] R. Gu, X.L. Gong,W.Q. Jiang, L.Y. Hao, S.H. Xuan, Z. Zhang, Synthesis and rheological investigation of a magnetic fluid using olivary silica-coated iron particles as a precursor, J. Magn. Magn. Mater. 320 (2008) 2788–2791.
[14] S. Yu, G.M. Chow, Carboxyl group (-CO2H) functionalized ferrimagnetic iron oxide nanoparticles for potential bio-applications, J. Mater. Chem. 14 (2004) 2781–2786.
[15] J. Fresnais, M. Yan, J. Courtois, T. Bostelmann, A. Bee, J.F. Berret, Poly(acrylic acid)-coated iron oxide nanoparticles: Quantitative evaluation of the coating properties and applications for the removal of a pollutant dye, J. Colloid. Interface Sci. 395 (2013), 24–30.
[16] I. Šafařík, M. Štěpánek, M. Uchman, M. Šlouf, E. Baldíková, L. Nýdlová, K. Pospíšková, M. Šafaříková, Composite particles formed by complexation of poly(methacrylic acid)–stabilized magnetic fluid with chitosan: Magnetic material for bioapplications. Mater. Sci. Eng. C 2016, 67, 486–492.
[17] M. Klokkenburg, B.H. Erne, Comparison of reversible and irreversible dipolar assemblies in a ferrofluid, J. Magn. Magn. Mater. 306 (2006) 85–91.
[18] R. Sondjaja, T.A. Hatton, M.K.C. Tam, Clustering of magnetic nanoparticles using a double hydrophilic block copolymer, poly(ethylene oxide)-*b*-poly(acrylic acid), J. Magn. Magn. Mater. 321 (2009) 2393–2397.
[19] G. Basina, G. Mountrichas, E. Devlin, N. Boukos, D. Niarchos, D. Petridis, S. Pispas, V. Tzitzios, Synthesis and Magnetic Properties of Fe(3)O(4) Nanoparticles Coated with Biocompatible Double Hydrophilic Block Copolymer. J. Nanosci. Nanotechnol. 9 (2009) 4753–4759.
[20] J. Hajduová, M. Uchman, I. Šafařík, M. Šafaříková, M. Šlouf, S. Pispas, M. Štěpánek, Aggregation of superparamagnetic iron oxide nanoparticles in dilute aqueous dispersions: Effect of coating by double-hydrophilic block polyelectrolyte, Colloids. Surf. A Physicochem. Eng. Aspects 483 (2015) 1–7.
[21] D. Franke, A.G. Kikhney, D.I. Svergun, Automated acquisition and analysis of small angle X-ray scattering data, Nucl. Instruments Methods Phys. Res. A 689 (2012) 52–59.
[22] E.S. Milonas, D.I. Svergun, Accuracy of molecular mass determination of proteins in solution by small-angle X-ray scattering, J. Appl. Cryst. 40 (2007) 245–249.
[23] I. Bressler, J. Kohlbrecher, A.F. Thünemann, SASfit: a tool for small-angle scattering data analysis using a library of analytical expressions. J. Appl. Cryst. 48 (2015) 1587–1598.
[24] M.E. Fisher, R.J. Burford, Theory of Critical-Point Scattering and Correlations I. The Ising Model, Phys. Rev. A 156 (1967) 583–622.

[25] J. Teixeira, Small-angle scattering by fractal systems, J. Appl. Cryst. 21 (1988,) 781–785.

[26] L.F. Shen, A. Stachowiak, S.E.K. Fateen, P.E. Laibinis, T.A. Hatton, Structure of alkanoic acid stabilized magnetic fluids. A small-angle neutron and light scattering analysis, Langmuir 17 (2001) 288–299.